

Article

Relation Between the Defect Interactions and the Serration Dynamics in a Zr-Based Bulk Metallic Glass

Jamieson Brechtl¹, Zhong Wang², Xie Xie³, Jun-Wei Qiao² and Peter K. Liaw^{3,*} 

¹ The Bredesen Center for Interdisciplinary Research and Graduate Education, The University of Tennessee, Knoxville, TN 37996, USA; brechtljm@ornl.gov

² College of Materials Science and Engineering, Taiyuan University of Technology, Taiyuan 030024, China; zhongwangty@hotmail.com (Z.W.); qiaojunwei@gmail.com (J.-W.Q.)

³ Department of Materials Science and Engineering, The University of Tennessee, Knoxville, TN 37996, USA; xie.xie@fcagroup.com

* Correspondence: pliaw@utk.edu

Received: 30 April 2020; Accepted: 2 June 2020; Published: 4 June 2020



Abstract: For this study, the effects of thermal annealing and compressive strain rate on the complexity of the serration behavior in a Zr-based bulk metallic glass (BMG) was investigated. Here, as-cast and thermally-annealed (300 °C, 1 week) $Zr_{52.5}Cu_{17.9}Ni_{14.6}Al_{10}Ti_5$ BMG underwent room-temperature compression tests in the unconstrained condition at strain rates of $2 \times 10^{-5} s^{-1}$ and $2 \times 10^{-4} s^{-1}$. The complexity of the serrated flow was determined, using the refined composite multiscale entropy technique. Nanoindentation testing and X-ray diffraction characterization were performed to assess the changes in the microstructure and mechanical properties of the BMG that occurred during annealing. The results indicated that the BMG did not crystallize during annealing in the prescribed heating condition. Nanoindentation tests revealed that annealing led to a significant increase in the depth-dependent nanoindentation hardness and Young's modulus, which were attributed to the structural relaxation in the glass. Furthermore, both annealing and an increased strain rate resulted in a marked enhancement in the complexity of the serrated flow during compression. It was concluded that the increase in the sample entropy with increasing strain rate is related to an increase in the number of defect interactions during the serrated flow.

Keywords: bulk metallic glasses; serrated flow; microstructure; nanoindentation; X-ray diffraction

1. Introduction

Due to their desirable properties, such as high strength and strength-to-weight ratio, as well as good room-temperature wear and corrosion resistance [1–6], bulk metallic glasses (BMGs) are potential candidates for many industrial applications. Furthermore, BMGs have exhibited excellent combinations of strength and toughness that cannot be achieved by conventional metals [7]. Despite these positive aspects, brittle fracture features are still an issue for most BMGs [8].

Like crystalline materials, defects play an integral role during the plastic deformation in BMGs. For instance, plastic strain in BMGs is often localized into thin shear bands (~20 nm [9]) that can lead to cracking and subsequent fracture of the alloy [10]. Greer et al. suggested that shear bands can initiate from either the percolation of shear transformation zones (STZs) [11] or casting defects (such as voids and surface notches) that can act as nucleation sites [12]. In addition to shear bands and STZs, soft-zone (SZ) (or liquid-like zone [13]) defects can affect the deformation behavior of BMGs, since they can deflect or defer shear bands and crack propagation [14,15]. Furthermore, it has been reported that a loss of these defects, due to the thermally-induced structural relaxation, can lead to the embrittlement in BMGs [14].

One way that shear banding manifests itself in BMGs during plastic deformation is in the form of the serrated flow behavior [16–23]. This type of behavior is characterized by repeated cycles of a sudden stress drop followed by an elastic reloading [24], and is typically associated with significant changes in the microstructure [25,26]. The serrated flow in BMGs can be affected by extrinsic parameters, such as the strain rate and temperature, or intrinsic properties, including the elastic modulus [16,27,28]. For instance, serrations can be inhibited at low temperatures or high strain rates [29].

Different types of analytical techniques have been used to analyze the serration behavior in BMGs. These methods include the mean field theory technique [16,17,30], statistical analysis methods [31], and complexity analysis techniques [23]. One such complexity technique is known as the refined composite multiscale entropy (RCMSE) method, which estimates the degree of complexity of time-series data [32]. Higher complexity values (sample entropy) are typically characteristic of a less predictable time series, while lower values typically indicate that a time series is more regular [33]. The higher complexity values have also been attributed to a higher degree of “meaningful structural richness” [34]. In physiology, the complexity of a time series is indicative of the ability of a biological system to adapt and function in an ever-changing environment [35]. As for the serrated flow in alloys, higher complexity values have been attributed to a greater variety of defect interactions, which is indicative of more complex behavior [23,36,37]. For instance, it was reported that in a $Zr_{55}Cu_{30}Ni_5Al_{10}$ BMG, the increase in the complexity values for the serration behavior corresponded to the creation and interaction of more SZ defects at the higher strain rates [23].

The purpose of the current investigation is to expand upon the work done in [23]. More specifically, the present work will examine how the thermally-induced structural relaxation affects the dynamical complexity of the serration behavior in a similar Zr-based BMG during compression. Importantly, it is believed that this study will build upon the previous knowledge regarding the influence of structural relaxation on the dynamics of the serrated flow.

2. Materials and Methods

2.1. Mechanical and Microstructural Characterization

The $Zr_{52.5}Cu_{17.9}Ni_{14.6}Al_{10}Ti_5$ BMG (also known as BAM-11) in atomic percent was fabricated at the University of Tennessee by arc melting in a Ti-gettered argon atmosphere, using a mixture of base pure metals (weight purity $\geq 99.9\%$). The ingots were remelted at least four times, to ensure the compositional homogeneity. Subsequently, the cylindrical rod samples with a diameter of 3 mm and a length of about 60 mm were prepared by suction casting into a water-cooled copper mold. The alloys were then remelted and drop cast in a Zr-gettered helium atmosphere. Subsequently, the rod was remelted and drop cast into a water-cooled 7-mm-diameter cylindrical Cu mold contained within a Zr-gettered helium atmosphere. After fabrication, 6-mm-long samples were cut from the rod using a diamond saw. To examine the effects of thermal annealing on the mechanical behavior, samples were encased in a vacuum-evacuated quartz tube and subsequently annealed. The annealing condition was 300 °C (ramp rate of 5 °C/min) for one week. The above temperature was chosen since it is well below the reported glass transition temperature (393 °C [38]) of the alloy.

Bulk X-ray diffraction (XRD) was performed on the as-cast and thermally-annealed specimens at the Joint Institute for Advanced Materials (JIAM) Diffraction Facility at the University of Tennessee. The XRD was performed using a PANalytical Empyrean diffractometer equipped with a Xe proportional detector that employed the powder Bragg–Brentano geometry. The X-ray consisted of a Cu beam with a K-alpha wavelength of 1.54 Å, in addition to an accelerating voltage and current of 45 kV and 40 mA. The diffraction angle, 2θ , ranged between 20–80°, in which data was recorded every 0.013 degrees. Before running the experiment, samples were placed on a zero-background holder to shield out any diffraction patterns that were not associated with the sample.

Room-temperature nanoindentation hardness and Young’s modulus measurements were performed using a KLA-Tencor G200 Nano-indenter with a Berkovich 3-sided pyramidal diamond

tip in a continuous stiffness-measurement mode with a constant loading rate of $400 \mu\text{N s}^{-1}$. Before indenting, samples were polished to a mirror finish using colloidal silica (50 nm). The hardness and Young’s modulus were measured as a function of depth from the point of contact of the nanoindenter tip with the surface to a depth of ~ 2000 nm. For each test, ~ 20 indents were performed, in which the indent was placed at least $50 \mu\text{m}$ from other indents, large scratches, and sample edges to avoid the effect of strain fields [39]. Hardness was calculated using the Oliver and Pharr method [40,41]. Due to the large data scatter that is associated with surface roughness, hardness and modulus values for depths below ~ 200 nm were omitted.

For the compression tests, the as-cast and thermally-annealed (300°C , 1 week) $\text{Zr}_{52.5}\text{Cu}_{17.9}\text{Ni}_{14.6}\text{Al}_{10}\text{Ti}_5$ BMG specimens underwent room-temperature compression tests at strain rates of $2 \times 10^{-5} \text{ s}^{-1}$ and $2 \times 10^{-4} \text{ s}^{-1}$ using a computer-controlled MTS 810 materials testing machine. The samples had a length of 6 mm and diameter of 3 mm (unconstrained condition). Before testing, the two compression faces of each sample were carefully polished such that they were parallel to one other, ensuring adequate contact with the platens during compression. A data-acquisition rate of 100 Hz was used to record the stress vs. time measurements.

2.2. Refined Composite Multiscale Entropy Technique

Below is a basic outline describing how to apply the RCMSE technique to analyze the serration behavior:

- (1) First, eliminate the trend that arises in the strain-hardening regime [42]. This step can be accomplished by either fitting the data using either third order polynomial or moving average methods, and then subtracting the fit from the original data set [43]. One can next define the k th coarse-grained time series from the detrended data set, $y_{k,j}^\tau$ [32]:

$$y_{k,j}^\tau = \frac{1}{\tau} \sum_{i=(j-1)\tau+k}^{j\tau+k-1} x_i \quad ; \quad 1 \leq j \leq \frac{N}{\tau} \quad , \quad 1 \leq k \leq \tau \quad (1)$$

where x_i is the i th point from the detrended time-series data, N is the total number of data points from the series data, τ is the scale factor, and k is an indexing factor that designates at which data point in the series to begin the analysis.

- (2) Write the time series of y_k^τ as a vector for each τ :

$$\mathbf{y}_k^\tau = \{ y_{k,1}^\tau \quad y_{k,2}^\tau \quad \dots \quad y_{k,M}^\tau \} \quad (2)$$

where $M = N/\tau$ and each $y_{k,j}^\tau$ is determined using Equation (1).

- (3) Construct the template vectors of dimension m , (typically $m = 2$):

$$\mathbf{y}_{k,i}^{\tau,m} = \{ y_{k,i}^\tau \quad y_{k,i+1}^\tau \quad \dots \quad y_{k,i+m-1}^\tau \} \quad ; \quad 1 \leq i \leq N - m \quad ; \quad 1 \leq k \leq \tau \quad (3)$$

- (4) Determine whether two template vectors match by measuring the distance between them via the infinity norm [44]:

$$d_{jl}^{\tau,m} = \left\| \mathbf{y}_j^{\tau,m} - \mathbf{y}_l^{\tau,m} \right\|_\infty = \max \left\{ \left| y_{1,j}^\tau - y_{1,l}^\tau \right| \dots \left| y_{i+m-1,j}^\tau - y_{i+m-1,l}^\tau \right| \right\} < r \quad (4)$$

where r is a predefined tolerance value, defined as r is chosen as 0.15 times of the standard deviation of the data [33,34,45]. This value of r is chosen since it imposes a normalization effect on the data such that the sample entropy will not depend on its variance [46]. If $d_{jl}^{\tau,m}$ is less than r , the two vectors will match.

- (5) Repeat steps (1–4) for $m = m + 1$.
- (6) Calculate the RCMSE value (typically denoted as the sample entropy) for a given τ by first summing the number of matching pairs for each $m, m + 1$ from $k = 1$ to τ and then taking the logarithm of their ratios, as shown in the following equation [32]:

$$RCMSE(\mathbf{X}, \tau, m, r) = \text{Ln} \left(\frac{\sum_{k=1}^{\tau} n_{k,\tau}^m}{\sum_{k=1}^{\tau} n_{k,\tau}^{m+1}} \right) \quad (5)$$

where $n_{k,\tau}^m$ and $n_{k,\tau}^{m+1}$ are the number of matching for a given k, τ , and m .

3. Results

Figure 1 presents the bulk XRD patterns for the as-cast and annealed samples (300 °C for 1 week) for scattering angles ranging from 20 to 80°. For the figure, both patterns exhibit a broad hump that does not contain any distinct, sharp peaks. The above result indicates that the BMG retained an amorphous structure during annealing. It is important to note that the exhibited resistance to the crystallization of the BMG, during annealing at 300 °C, was also observed in a previous investigation [47].

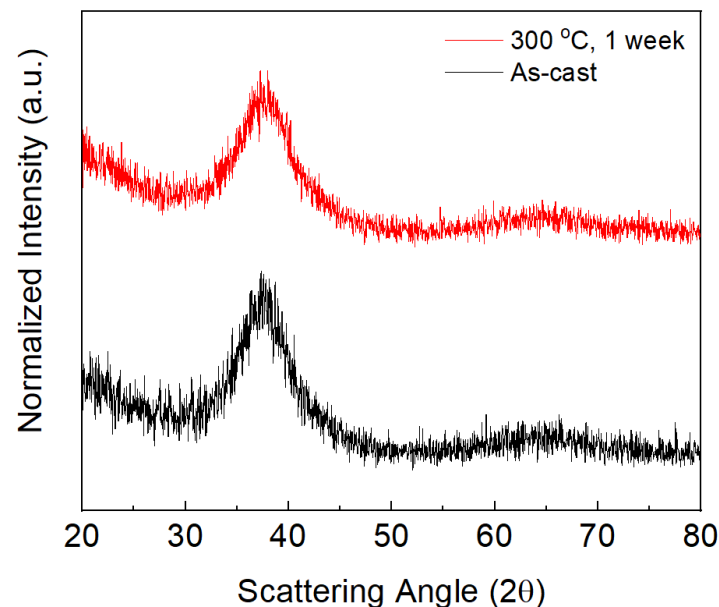


Figure 1. The XRD patterns for the as-cast and annealed $\text{Zr}_{52.5}\text{Cu}_{17.9}\text{Ni}_{14.6}\text{Al}_{10}\text{Ti}_5$ bulk metallic glass (BMG) samples.

Figure 2a,b displays the nanoindentation hardness and Young's modulus vs. indentation depth for the as-cast and thermally-annealed (300 °C, 1 week) $\text{Zr}_{52.5}\text{Cu}_{17.9}\text{Ni}_{14.6}\text{Al}_{10}\text{Ti}_5$ BMG specimens. As can be seen, the hardness and Young's modulus both decreased with an increase in the indentation depth. Furthermore, a pronounced indentation size effect can be seen, as indicated by the rapid increase in the measured hardness with decreasing indent depth. It was also found that the hardness and modulus values were significantly higher for the annealed samples at all indentation depths. This significant increase in both the hardness and modulus indicates that in the annealed sample, the short-range atomic rearrangement due to the structural relaxation of the glass occurred [47].

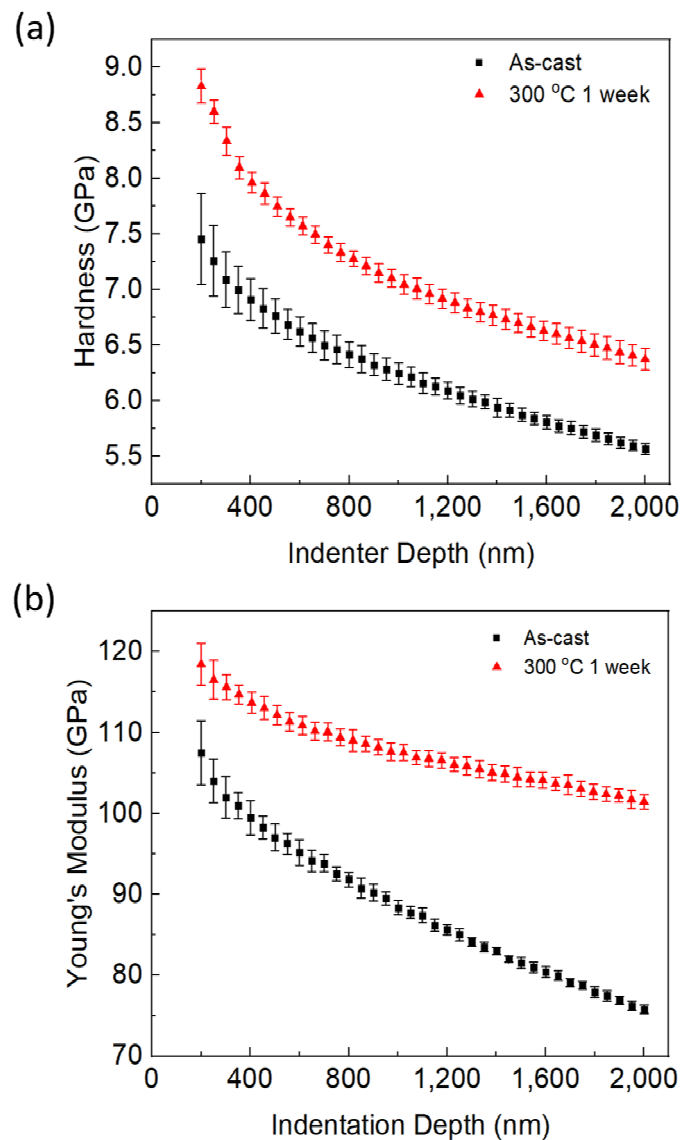


Figure 2. (a) Nanoindentation hardness vs. indentation depth for the as-cast and annealed (300 °C, 1 week) $Zr_{52.5}Cu_{17.9}Ni_{14.6}Al_{10}Ti_5$ BMG samples. (b) Nanoindentation Young's modulus vs. indentation depth for the as-cast and annealed (300 °C, 1 week) $Zr_{52.5}Cu_{17.9}Ni_{14.6}Al_{10}Ti_5$ BMG samples for indentations depths ranging from 200 to 2000 nm.

Figure 3a–d shows the detrended stress vs. time data for the as-cast and thermally-annealed (300 °C for 1 week) $Zr_{52.5}Cu_{17.9}Ni_{14.6}Al_{10}Ti_5$ BMGs that were compressed in the unconstrained condition at strain rates of $2 \times 10^{-5} \text{ s}^{-1}$ and $2 \times 10^{-4} \text{ s}^{-1}$. As can be seen, the serrated flow curves for the annealed samples consist of a more irregular structure, compared to the as-cast sample. For instance, the serration curves for the annealed samples contain a greater number of relatively smaller fluctuations (stress drops) that are interspersed within the greater stress drops. The smaller fluctuations likely correspond to the secondary shear banding [48]. Furthermore, the elapsed time between serrations is significantly shorter for the samples compressed at the higher strain rate in Figure 3a,b, indicating that the frequency of serrations is greater in this condition.

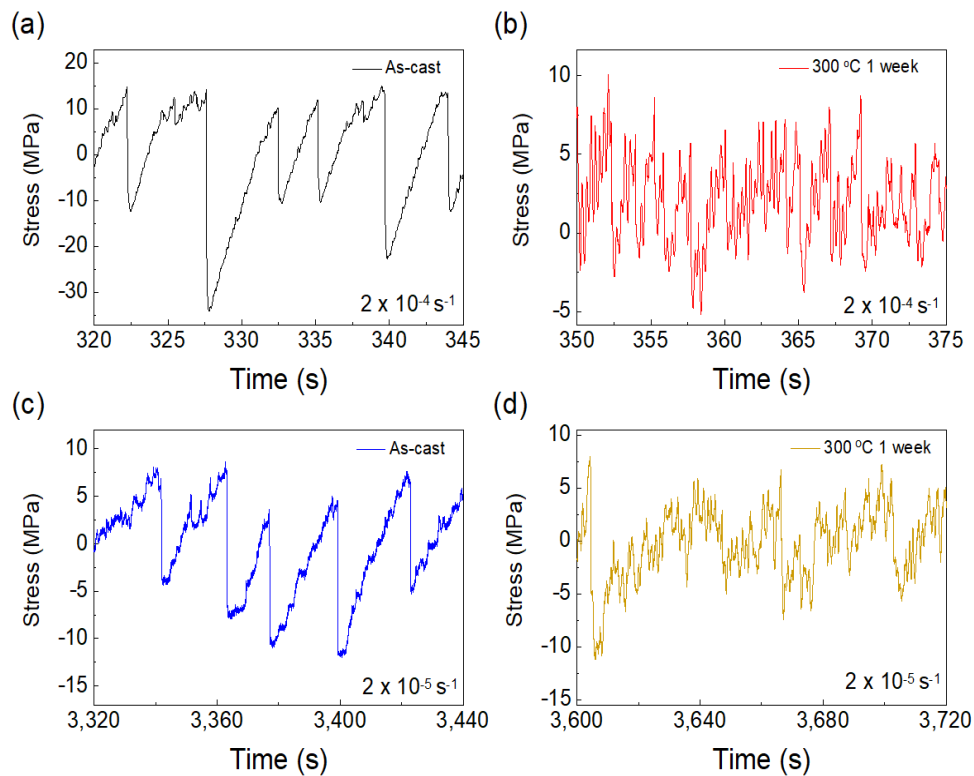


Figure 3. Graphs for the detrended stress vs. time curves for the (a) as-cast $Zr_{52.5}Cu_{17.9}Ni_{14.6}Al_{10}Ti_5$ BMG compressed at a strain rate of $2 \times 10^{-4} s^{-1}$, (b) thermally-annealed (300 °C, 1 week) $Zr_{52.5}Cu_{17.9}Ni_{14.6}Al_{10}Ti_5$ BMG compressed at a strain rate of $2 \times 10^{-4} s^{-1}$, (c) as-cast $Zr_{52.5}Cu_{17.9}Ni_{14.6}Al_{10}Ti_5$ BMG compressed at a strain rate of $2 \times 10^{-5} s^{-1}$, and (d) thermally-annealed (300 °C, 1 week) $Zr_{52.5}Cu_{17.9}Ni_{14.6}Al_{10}Ti_5$ BMG compressed at a strain rate of $2 \times 10^{-5} s^{-1}$.

Figure 4a–d displays the results of the complexity modeling and analysis for the as-cast and annealed $Zr_{52.5}Cu_{17.9}Ni_{14.6}Al_{10}Ti_5$ BMG specimens compressed at strain rates of $2 \times 10^{-5} s^{-1}$ and 2×10^{-4} . For all the graphs, the sample-entropy values increased with increasing scale factor. This result indicates that for all the experimental conditions, the serrated flow exhibits complex behavior across multiple scales [34]. Furthermore, the sample-entropy curves were affected by both annealing and strain rate. As displayed in Figure 4a,b, the sample-entropy curves were significantly higher for the samples that were annealed. As for the strain rate, the curves were markedly greater for the higher strain rate condition (see Figure 4c,d). This increase in the sample entropy with an increasing strain rate was also observed in [23]. Finally, from the graphs, it is apparent that the annealed sample that was compressed at the highest strain rate exhibited the greatest sample-entropy values, as compared to all the other conditions. Conversely, the as-cast sample that was compressed at the lowest strain rate exhibited the lowest values.

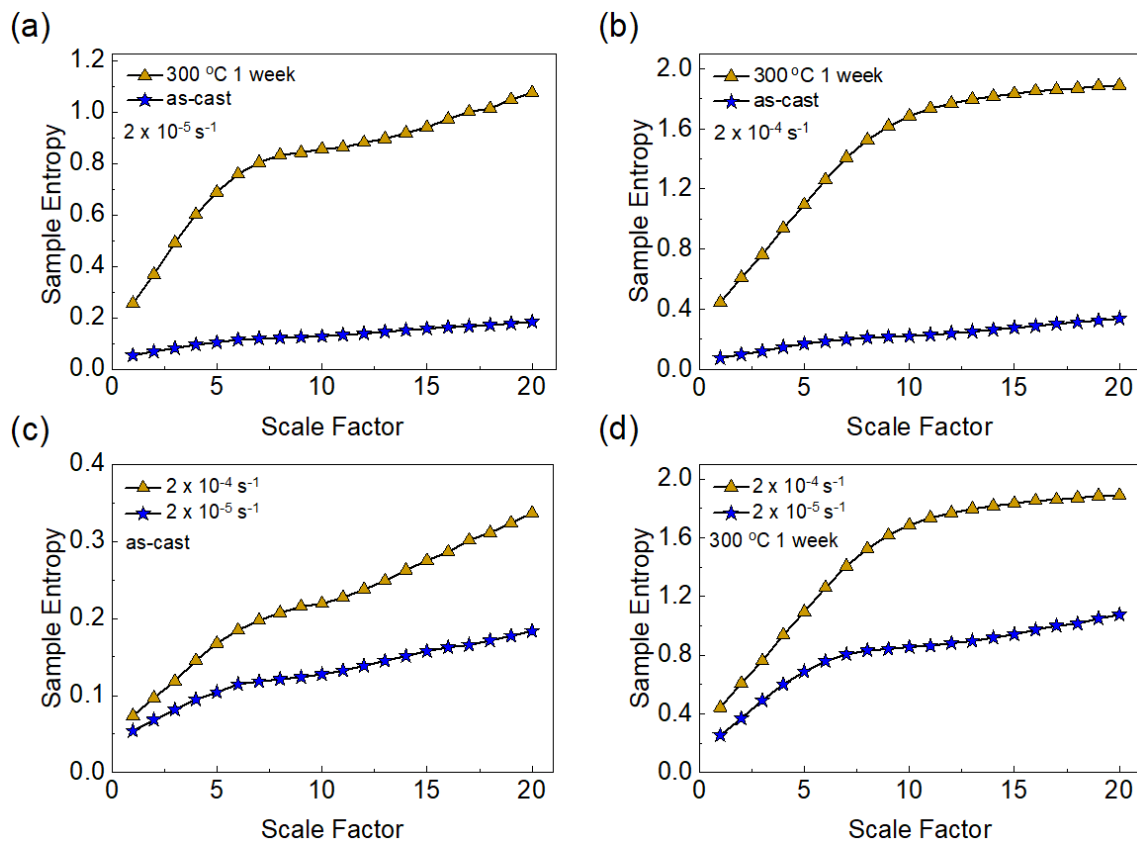


Figure 4. A comparison of the sample entropy vs. the scale factor for the (a) as-cast and annealed (300 °C, 1 week) $\text{Zr}_{52.5}\text{Cu}_{17.9}\text{Ni}_{14.6}\text{Al}_{10}\text{Ti}_5$ BMG specimen that was compressed at a strain rate of $2 \times 10^{-5} \text{ s}^{-1}$, (b) as-cast and annealed (300 °C, 1 week) $\text{Zr}_{52.5}\text{Cu}_{17.9}\text{Ni}_{14.6}\text{Al}_{10}\text{Ti}_5$ BMG specimen that was compressed at a strain rate of $2 \times 10^{-4} \text{ s}^{-1}$, (c) as-cast samples compressed at strain rates of $2 \times 10^{-5} \text{ s}^{-1}$ and $2 \times 10^{-4} \text{ s}^{-1}$, and (d) the annealed sample (300 °C, 1 week) compressed at strain rates of $2 \times 10^{-5} \text{ s}^{-1}$ and $2 \times 10^{-4} \text{ s}^{-1}$.

To quantitatively analyze and compare the data from Figure 4a–d, the area enclosed under the sample-entropy curves (denoted as A_{SE}) was calculated. Here, a greater A_{SE} value corresponds to a time series that is relatively more complex [49]. The results of the analysis are tabulated in Table 1. From the table, a few things can be inferred. For both the as-cast and the annealed samples, the A_{SE} values increased with respect to the applied strain rate. Here, the A_{SE} value increased for the as-cast and the annealed samples by 75% and 85%, respectively. Furthermore, for both strain rates, the A_{SE} was markedly higher for the annealed sample.

Table 1. Comparison of the A_{SE} value for the as-cast and thermally annealed (300 °C, 1 week) $\text{Zr}_{52.5}\text{Cu}_{17.9}\text{Ni}_{14.6}\text{Al}_{10}\text{Ti}_5$ BMG, for strain rates of $2 \times 10^{-5} \text{ s}^{-1}$ and $2 \times 10^{-4} \text{ s}^{-1}$.

Sample Condition	Strain Rate (s^{-1})	A_{SE}
As-cast	2×10^{-5}	2.4
	2×10^{-4}	4.2
300 °C, 1 week	2×10^{-5}	15.4
	2×10^{-4}	28.5

4. Discussion

For this investigation, the effects of annealing and strain rate on the microstructure and mechanical behavior of a $\text{Zr}_{52.5}\text{Cu}_{17.9}\text{Ni}_{14.6}\text{Al}_{10}\text{Ti}_5$ BMG were examined. The microstructure was examined using

the bulk XRD, while nanoindentation and compression experiments were employed to examine the deformation behavior. Importantly, the XRD results (see Figure 1) suggest that the alloy did not crystallize during annealing at 300 °C for one week. This result is corroborated by a previous investigation, which found that the same alloy did not crystallize during annealing at 300 °C for up to two weeks [47].

As observed in Figure 2a, annealing the specimen at 300 °C for 1 week was found to significantly increase the nanoindentation hardness of the alloy. This increase in the hardness arises from the thermally-induced structural relaxation of the alloy. Moreover, the structural relaxation is a consequence of the thermal annihilation of the SZ defects in the alloy [47]. For example, Li et al. estimated that in the $Zr_{52.5}Cu_{17.9}Ni_{14.6}Al_{10}Ti_5$ BMG, annealing at 300 °C for 1 week (the same alloy and thermal conditions as the present study) reduced the density of these defects by almost two orders of magnitude [14]. These defects consist of loosely-packed regions and structural heterogeneities that can accommodate shear deformation under an applied load, relative to the glass matrix [15]. Moreover, the loss of SZ defects during structural relaxation can result in an increased difficulty of shear-band initiation. Consequently, their destruction would lead to an increased resistance to deformation that corresponds to an increase in the hardness.

Similar to the hardness results, the nanoindentation Young's modulus (see Figure 2b) also significantly increased during annealing. The increase in the modulus is accompanied by a decrease in the interatomic spacing. It has been shown that an increase in the interatomic spacings, via structural rejuvenation, results in an increase in the number of liquid-like sites (or SZ defects) in the glass [50,51]. Therefore, the converse should also hold true, i.e., a decrease in the interatomic distance caused by thermally-induced structural relaxation will result in fewer SZ defects. This hypothesis is corroborated by Li et al. [14], where it was reported that the structural relaxation led to a decrease in the SZ defect density of the $Zr_{52.5}Cu_{17.9}Ni_{14.6}Al_{10}Ti_5$ BMG. Thus, the increase in the Young's modulus of the alloy is linked to the annihilation of the SZ defects during thermal annealing.

As shown in Figure 4a–d, the sample-entropy curves increased with an increase in the scale factor for all the experimental conditions. This result indicates that for the $Zr_{52.5}Cu_{17.9}Ni_{14.6}Al_{10}Ti_5$ BMG, the serrations exhibited complex behavior during compression. Additionally, the complexity of the serrated flow, as indicated by the sample-entropy values, was affected by both the microstructural changes induced by thermal annealing, as well as the strain rate. In terms of the former, the sample-entropy curves, as well as the A_{SE} values (see Figure 4a–d and Table 1), for the samples annealed at 300 °C for 1 week were significantly greater, compared to the as-cast sample. Based on Figure 3a–d, this higher degree of complexity (or dynamical richness) is characterized by the more irregular serration structure that can be observed in the stress vs. time graphs. The markedly higher sample entropy for annealed specimens indicates that the serrated flow exhibits complex behavior that contains a higher degree of “meaningful structural richness” [34].

Previous investigations involving both crystalline and amorphous alloys reported that the degree of complexity exhibited by the serrated flow increases with an increase in the variety, number, and rate of defect interactions that occur during the serrated flow [23,36,37]. In the carburized steel, for example, an increase in the complexity (sample entropy) of the serrated flow was due to a larger number of locking interactions that occurred between the carbon impurities and the dislocations during tension [36]. In a study that examined the compression behavior of the $Zr_{55}Cu_{30}Ni_5Al_{10}$ BMG, the sample entropy increased with increasing applied strain rate [23]. It was hypothesized that the increase in the complexity of the serration behavior resulted from a rise in the interaction rate between free-volume and anti-free volume defects.

Importantly, the annihilation of the SZ defects is accompanied by a decrease in the initiation of shear bands [15]. This decrease in the quantity of defects suggests that, compared to the as-cast sample, the complexity of the serrated flow should be lower for the annealed specimen. This discrepancy may be explained by the following. In a previous investigation, it was observed that in an annealed Zr-Cr-Fe-Al BMG, secondary shear bands were localized in the vicinity of a dominant shear band after

compression testing [52]. The above result was in contrast with the as-cast sample, where the shear bands were more widely distributed within the sample. This wider distribution of the shear bands suggests that the shear-band initiation occurred randomly throughout the material. If we apply the above ideas to the present study, it is likely that the shear banding occurred in the as-cast sample in a more random fashion during the serrated flow. Thus, the stick-slip events probably occurred randomly throughout the glassy matrix. Such random behavior is indicative of serrations that are less spatially correlated, and therefore less complex in nature [53].

In the annealed samples, on the other hand, the secondary shear bands were more localized to one shear band, and thus more spatially correlated. Furthermore, the more rapid onset of serrations, due to the secondary shear banding (see Figure 3b,d), indicates there may be less time for the alloy to accommodate the plastic load. This decrease in the plastic relaxation time between successive drops increases the chance that recurrent plastic events will overlap, resulting in a hierarchy of length scales [46]. Thus, the annealed samples exhibit serrations that have a greater degree of spatiotemporal correlations, which is indicative of more complex dynamical behavior.

In terms of the strain rate, it is likely that the dynamical complexity increased due to the increased rate of defect interactions. However, the type of defect interactions that occurred were different for the as-cast and thermally-annealed samples. For the as-cast sample, an increase in the strain rate leads to the creation of free volumes and SZ defects [23,54]. As a result, there are more defects in the glassy matrix that can interact, leading to a greater variety of interactions during the serrated flow. In contrast, the increase in the sample entropy in the annealed samples with increasing strain rate is probably due to an increase in the number of secondary shear-band interactions that occur during the serrated flow.

5. Conclusions

For this investigation, the as-cast and thermally-annealed (300 °C, 1 week) $Zr_{52.5}Cu_{17.9}Ni_{14.6}Al_{10}Ti_5$ BMG underwent room-temperature compression tests in the unconstrained condition at strain rates of $2 \times 10^{-5} \text{ s}^{-1}$ and $2 \times 10^{-4} \text{ s}^{-1}$. The X-ray diffraction characterization indicated that the BMG did not crystallize during annealing in the prescribed heating condition. The results of nanoindentation testing indicate that annealing led to the annihilation of SZ defects from the glass. Furthermore, it was observed that both annealing and an increased strain rate resulted in a marked increase in the sample-entropy values for the serrated flow exhibited by the BMG during compression. As for the former, it is believed that the reduction of SZ defects is accompanied by secondary shear-banding behavior that is more spatially correlated, resulting in more complex dynamical behavior during the serrated flow. In terms of the latter, the increase in the sample entropy with increasing strain rate is related to an increase in the number of defect interactions. In the context of the as-cast sample, there was an increase in the interactions between SZ defects, while for the annealed sample more secondary shear-band interactions were involved during the serrated flow.

Author Contributions: Conceptualization: J.B., Z.W., J.-W.Q. and P.K.L.; data curation: Z.W.; formal analysis: J.B. and X.X.; funding acquisition: P.K.L.; investigation: J.B. and Z.W.; methodology: J.B. and Z.W.; resources: Z.W. and X.X.; software: X.X.; supervision: P.K.L.; validation: Z.W. and X.X.; visualization: J.B.; writing—original draft: J.B. and Z.W.; writing—review and editing: J.B., J.-W.Q. and P.K.L. All authors have read and agreed to the published version of the manuscript.

Funding: Xie Xie and Peter K. Liaw are thankful for the support from the National Science Foundation (DMR 1611180 and 1809640), and the program directors, Dr. J. Yang, Dr. G. Shiflet, and Dr. D. Farkas.

Acknowledgments: The authors would like to thank Michael Koehler for useful discussions regarding the X-ray diffraction experiments and UT's Joint Institute for Advanced Materials.

Conflicts of Interest: The authors declare no conflict of interest.

References

1. Telford, M. The case for bulk metallic glass. *Mater. Today* **2004**, *7*, 36–43. [[CrossRef](#)]
2. Schuh, C.A.; Hufnagel, T.C.; Ramamurty, U. Overview No.144 - Mechanical behavior of amorphous alloys. *Acta Mater.* **2007**, *55*, 4067–4109. [[CrossRef](#)]
3. Madge, S.V.; Caron, A.; Gralla, R.; Wilde, G.; Mishra, S.K. Novel W-based metallic glass with high hardness and wear resistance. *Intermetallics* **2014**, *47*, 6–10. [[CrossRef](#)]
4. Greer, A.L.; Rutherford, K.L.; Hutchings, I.M. Wear resistance of amorphous alloys and related materials. *Int. Mater. Rev.* **2002**, *47*, 87–112. [[CrossRef](#)]
5. Peter, W.H.; Buchanan, R.A.; Liu, C.T.; Liaw, P.K.; Morrison, M.L.; Horton, J.A.; Carmichael, C.; Wright, J.L. Localized Corrosion behavior of a zirconium-based bulk metallic glass relative to its crystalline state. *Intermetallics* **2002**, *10*, 1157–1162. [[CrossRef](#)]
6. Hua, N.; Huang, L.; Wang, J.; Cao, Y.; He, W.; Pang, S.; Zhang, T. Corrosion behavior and in vitro biocompatibility of Zr–Al–Co–Ag bulk metallic glasses: An experimental case study. *J. Non-Cryst. Solids* **2012**, *358*, 1599–1604. [[CrossRef](#)]
7. Kruzic, J.J. Bulk Metallic Glasses as Structural Materials: A Review. *Adv. Eng. Mater.* **2016**, *18*, 1308–1331. [[CrossRef](#)]
8. Madge, S.V. Toughness of Bulk Metallic Glasses. *Metals* **2015**, *5*, 1279–1305. [[CrossRef](#)]
9. Masumoto, T.; Maddin, R. Mechanical properties of palladium 20 at/o silicon alloy quenched from liquid state. *Acta Metall. Mater.* **1971**, *19*, 725–741. [[CrossRef](#)]
10. Wang, J.G.; Hu, Y.C.; Guan, P.F.; Song, K.K.; Wang, L.; Wang, G.; Pan, Y.; Sarac, B.; Eckert, J. Hardening of shear band in metallic glass. *Sci. Rep.* **2017**, *7*, 7076. [[CrossRef](#)]
11. Miller, M.; Liaw, P.K. (Eds.) *Bulk Metallic Glasses: An Overview*; Springer: New York, NY, USA, 2008.
12. Greer, A.L.; Cheng, Y.Q.; Maj, E. Shear bands in metallic glasses. *Mater. Sci. Eng. R Rep.* **2013**, *74*, 71–132. [[CrossRef](#)]
13. Egami, T. Mechanical failure and glass transition in metallic glasses. *J. Alloys Compd.* **2011**, *509*, S82–S86. [[CrossRef](#)]
14. Li, W.; Gao, Y.; Bei, H. On the correlation between microscopic structural heterogeneity and embrittlement behavior in metallic glasses. *Sci. Rep.* **2015**, *5*, 14786. [[CrossRef](#)]
15. Li, W.; Bei, H.; Tong, Y.; Dmowski, W.; Gao, Y.F. Structural heterogeneity induced plasticity in bulk metallic glasses: From well-relaxed fragile glass to metal-like behavior. *Appl. Phys. Lett.* **2013**, *103*, 171910. [[CrossRef](#)]
16. Antonaglia, J.; Xie, X.; Schwarz, G.; Wraith, M.; Qiao, J.; Zhang, Y.; Liaw, P.K.; Uhl, J.T.; Dahmen, K.A. Tuned critical avalanche scaling in bulk metallic glasses. *Sci. Rep.* **2014**, *4*, 4382. [[CrossRef](#)] [[PubMed](#)]
17. Antonaglia, J.; Wright, W.J.; Gu, X.; Byer, R.R.; Hufnagel, T.C.; LeBlanc, M.; Uhl, J.T.; Dahmen, K.A. Bulk metallic glasses deform via slip avalanches. *Phys. Rev. Lett.* **2014**, *112*, 1–5. [[CrossRef](#)] [[PubMed](#)]
18. Li, J.J.; Wang, Z.; Qiao, J.W. Power-law scaling between mean stress drops and strain rates in bulk metallic glasses. *Mater. Des.* **2016**, *99*, 427–432. [[CrossRef](#)]
19. Torre, F.H.D.; Klaumünzer, D.; Maaß, R.; Löffler, J.F. Stick–slip behavior of serrated flow during inhomogeneous deformation of bulk metallic glasses. *Acta Mater.* **2010**, *58*, 3742–3750. [[CrossRef](#)]
20. Maaß, R.; Klaumünzer, D.; Löffler, J.F. Propagation dynamics of individual shear bands during inhomogeneous flow in a Zr-based bulk metallic glass. *Acta Mater.* **2011**, *59*, 3205–3213. [[CrossRef](#)]
21. Shi, B.; Luan, S.Y.; Jin, P.P. Crossover from free propagation to cooperative motions of shear bands and its effect on serrated flow in metallic glass. *J. Non-Cryst. Solids* **2018**, *482*, 126–131. [[CrossRef](#)]
22. Jiang, W.H.; Fan, G.J.; Liu, F.X.; Wang, G.Y.; Choo, H.; Liaw, P.K. Spatiotemporally inhomogeneous plastic flow of a bulk-metallic glass. *Int. J. Plast.* **2008**, *24*, 1–16. [[CrossRef](#)]
23. Brechtel, J.; Xie, X.; Wang, Z.; Qiao, J.; Liaw, P.K. Complexity analysis of serrated flows in a bulk metallic glass under constrained and unconstrained conditions. *Mater. Sci. Eng.* **2020**, *771*, 138585. [[CrossRef](#)]
24. Alrasheedi, N.H.; Yousfi, M.A.; Hajlaoui, K.; Mahfoudh, B.J.; Tourki, Z.; Yavari, A.R. On the Modelling of the Transient Flow Behavior of Metallic Glasses: Analogy with Portevin-Le Chatelier Effect. *Metals* **2016**, *6*, 8. [[CrossRef](#)]
25. Zhang, Y.; Zuo, T.T.; Tang, Z.; Gao, M.C.; Dahmen, K.A.; Liaw, P.K.; Lu, Z.P. Microstructures and properties of high-entropy alloys. *Prog. Mater. Sci.* **2014**, *61*, 1–93. [[CrossRef](#)]

26. Niu, S.; Kou, H.; Zhang, Y.; Wang, J.; Li, J. The characteristics of serration in Al_{0.5}CoCrFeNi high entropy alloy. *Mater. Sci. Eng. A* **2017**, *702*, 96–103. [[CrossRef](#)]
27. Fan, Z.; Li, Q.; Fan, C.; Wang, H.; Zhang, X. Strategies to tailor serrated flows in metallic glasses. *J. Mater. Res.* **2019**, *34*, 1595–1607. [[CrossRef](#)]
28. Sun, B.A.; Pauly, S.; Tan, J.; Stoica, M.; Wang, W.H.; Kuhn, U.; Eckert, J. Serrated flow and stick-slip deformation dynamics in the presence of shear-band interactions for a Zr-based metallic glass. *Acta Mater.* **2012**, *60*, 4160–4171. [[CrossRef](#)]
29. Wang, Y.T.; Dong, J.; Liu, Y.H.; Bai, H.Y.; Wang, W.H.; Sun, B.A. Optimum shear stability at intermittent-to-smooth transition of plastic flow in metallic glasses at cryogenic temperatures. *Materialia* **2020**, *9*, 100559. [[CrossRef](#)]
30. Wright, W.J.; Long, A.A.; Gu, X.J.; Liu, X.; Hufnagel, T.C.; Dahmen, K.A. Slip statistics for a bulk metallic glass composite reflect its ductility. *J. Appl. Phys.* **2018**, *124*, 8. [[CrossRef](#)]
31. Ren, J.L.; Chen, C.; Wang, G.; Mattern, N.; Eckert, J. Dynamics of serrated flow in a bulk metallic glass. *AIP Adv.* **2011**, *1*, 032158. [[CrossRef](#)]
32. Wu, S.-D.; Wu, C.-W.; Lin, S.-G.; Lee, K.-Y.; Peng, C.-K. Analysis of complex time series using refined composite multiscale entropy. *Phys. Lett. A* **2014**, *378*, 1369–1374. [[CrossRef](#)]
33. Costa, M.; Goldberger, A.L.; Peng, C.K. Multiscale entropy analysis of complex physiologic time series. *Phys. Rev. Lett.* **2002**, *89*, 068102. [[CrossRef](#)] [[PubMed](#)]
34. Costa, M.; Goldberger, A.L.; Peng, C.K. Multiscale entropy analysis of biological signals. *Phys. Rev. E* **2005**, *71*, 021906. [[CrossRef](#)] [[PubMed](#)]
35. Humeau-Heurtier, A. *Evaluation of Systems' Irregularity and Complexity: Sample Entropy, Its Derivatives, and Their Applications across Scales and Disciplines*; MDPI AG: Basel, Switzerland, 2018.
36. Brechtel, J.; Chen, B.; Xie, X.; Ren, Y.; Venable, J.D.; Liaw, P.K.; Zinkle, S.J. Entropy modeling on serrated flows in carburized steels. *Mater. Sci. Eng. A* **2019**, *753*, 135–145. [[CrossRef](#)]
37. Sarkar, A.; Chatterjee, A.; Barat, P.; Mukherjee, P. Comparative study of the Portevin-Le Chatelier effect in interstitial and substitutional alloy. *Mater. Sci. Eng. A-Struct. Mater. Prop. Microstruct. Process.* **2007**, *459*, 361–365. [[CrossRef](#)]
38. Perez-Bergquist, A.G.; Bei, H.; Leonard, K.J.; Zhang, Y.; Zinkle, S.J. Effects of ion irradiation on Zr_{52.5}Cu_{17.9}Ni_{14.6}Al₁₀Ti₅ (BAM-11) bulk metallic glass. *Intermetallics* **2014**, *53*, 62–66. [[CrossRef](#)]
39. Clark, D.W.; Zinkle, S.J.; Patel, M.K.; Parish, C.M. High temperature ion irradiation effects in MAX phase ceramics. *Acta Mater.* **2016**, *105*, 130–146. [[CrossRef](#)]
40. Oliver, W.C.; Pharr, G.M. An improved technique for determining hardness and elastic modulus using load and displacement sensing indentation experiments. *J. Mater. Res.* **1992**, *7*, 1564–1583. [[CrossRef](#)]
41. Oliver, W.C.; Pharr, G.M. Measurement of hardness and elastic modulus by instrumented indentation: Advances in understanding and refinements to methodology. *J. Mater. Res.* **2004**, *19*, 3–20. [[CrossRef](#)]
42. Sarkar, A.; Maloy, S.A.; Murty, K.L. Investigation of Portevin-LeChatelier effect in HT-9 steel. *Mater. Sci. Eng. A* **2015**, *631*, 120–125. [[CrossRef](#)]
43. Iliopoulos, A.C.; Nikolaidis, N.S.; Aifantis, E.C. Analysis of serrations and shear bands fractality in UFGs. *J. Mech. Behav. Mater.* **2015**, *24*, 1–9. [[CrossRef](#)]
44. Brechtel, J.; Xie, X.; Liaw, P.K.; Zinkle, S.J. Complexity modeling and analysis of chaos and other fluctuating phenomena. *Chaos Solitons Fractals* **2018**, *116*, 166–175.
45. Costa, M.D.; Goldberger, A.L. Generalized multiscale entropy analysis: Application to quantifying the complex volatility of human heartbeat time series. *Entropy* **2015**, *17*, 1197–1203. [[CrossRef](#)] [[PubMed](#)]
46. Brechtel, J.; Chen, S.Y.; Xie, X.; Ren, Y.; Qiao, J.W.; Liaw, P.K.; Zinkle, S.J. Towards a greater understanding of serrated flows in an Al-containing high-entropy-based alloy. *Int. J. Plast.* **2019**, *115*, 71–92. [[CrossRef](#)]
47. Brechtel, J.; Wang, H.; Kumar, N.A.P.K.; Yang, T.; Lin, Y.R.; Bei, H.; Neuefeind, J.; Dmowski, W.; Zinkle, S.J. Investigation of the thermal and neutron irradiation response of BAM-11 bulk metallic glass. *J. Nucl. Mater.* **2019**, *526*, 151771. [[CrossRef](#)]
48. Huo, L.-S.; Wang, J.-Q.; Huo, J.-T.; Zhao, Y.-Y.; Men, H.; Chang, C.-T.; Wang, X.-M.; Li, R.-W. Interactions of Shear Bands in a Ductile Metallic Glass. *J. Iron Steel Res. Int.* **2016**, *23*, 48–52. [[CrossRef](#)]
49. Crespo, A.; Álvarez, D.; Gutiérrez-Tobal, G.C.; Vaquerizo-Villar, F.; Barroso-García, V.; Alonso-Álvarez, M.L.; Terán-Santos, J.; Hornero, R.; Campo, F.d. Multiscale entropy analysis of unattended oximetric recordings to assist in the screening of paediatric sleep apnoea at home. *Entropy* **2017**, *19*, 284. [[CrossRef](#)]

50. Egami, T.; Poon, S.J.; Zhang, Z.; Keppens, V. Glass transition in metallic glasses: A microscopic model of topological fluctuations in the bonding network. *Phys. Rev. B* **2007**, *76*, 6. [[CrossRef](#)]
51. Srolovitz, D.; Maeda, K.; Vitek, V.; Egami, T. Structural defects in amorphous solids Statistical analysis of a computer model. *Philos. Mag. A* **1981**, *44*, 847–866. [[CrossRef](#)]
52. Louzguine-Luzgin, D.V.; Jiang, J.; Bazlov, A.I.; Zolotarevsky, V.S.; Mao, H.; Ivanov, Y.P.; Greer, A.L. Phase separation process preventing thermal embrittlement of a Zr-Cu-Fe-Al bulk metallic glass. *Scr. Mater.* **2019**, *167*, 31–36. [[CrossRef](#)]
53. Sarkar, A.; Barat, P.; Mukherjee, P. Multiscale entropy analysis of the Portevin-Le Chatelier effect in an Al-2.5%Mg alloy. *Fractals* **2010**, *18*, 319–325. [[CrossRef](#)]
54. Yuan, B.; Li, J.-J.; Qiao, J.-W. Statistical analysis on strain-rate effects during serrations in a Zr-based bulk metallic glass. *J. Iron Steel Res. Int.* **2017**, *24*, 455–461. [[CrossRef](#)]



© 2020 by the authors. Licensee MDPI, Basel, Switzerland. This article is an open access article distributed under the terms and conditions of the Creative Commons Attribution (CC BY) license (<http://creativecommons.org/licenses/by/4.0/>).